Spatially resolved imaging spectroscopy with Solar Orbiter STIX

MIDAgroup

Università di Genova
DIMA | Dipartimento di Matematica

Anna Volpara, Paolo Massa, Andrea Francesco Battaglia,
Säm Krucker, Gordon Hurford, Michele Piana, Anna Maria Massone

---

Flare Forecasting Workshop
May 23, 2023

n|w

Università di Genova

STIX

Outline

1. From photon to electron visibilities
2. Visibility inversion algorithm
3. Results
4. Conclusions and future works

From photon to electron visibilities

Photon visibilities:

$$V(u, v; \epsilon) = \mathcal{F}(I(x, y; \epsilon)) = \int\int I(x, y; \epsilon) e^{2\pi i(xu+yv)}\, dx\, dy \qquad (1)$$

From photon to electron visibilities

Photon visibilities:

$$V(u, v; \epsilon) = \mathcal{F}(I(x, y; \epsilon)) = \int\int I(x, y; \epsilon) e^{2\pi i(xu+yv)}\, dx\, dy \tag{1}$$

Intensity of the X-ray photon flux emitted from (x, y) on the Sun

From photon to electron visibilities

Photon visibilities:

$$V(u, v; \epsilon) = \mathcal{F}(I(x, y; \epsilon)) = \int\int I(x, y; \epsilon) e^{2\pi i(xu+yv)}\, dx\, dy \qquad (1)$$

Array containing the N_V complex values of the visibilities measured by STIX

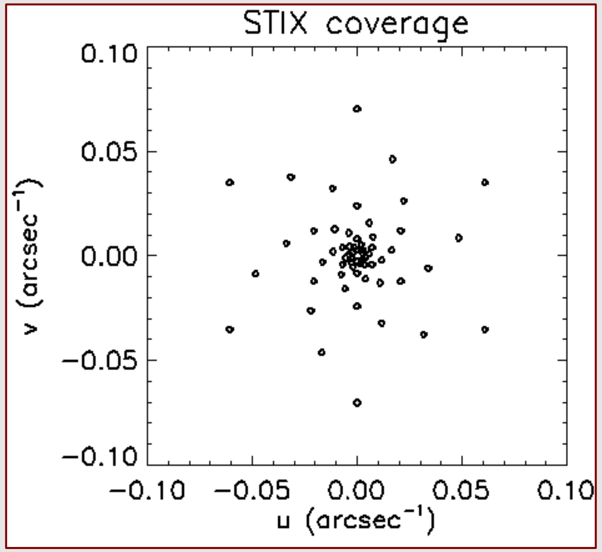

Figure: (u, v) frequencies sampled by STIX sub-collimators.

From photon to electron visibilities

Photon visibilities:

$$V(u, v; \epsilon) = \mathcal{F}(I(x, y; \epsilon)) = \int\int I(x, y; \epsilon) e^{2\pi i(xu+yv)}\, dx\, dy \qquad (1)$$

The Fourier Transform

From photon to electron visibilities

Photon visibilities:

$$V(u,v;\epsilon) = \mathcal{F}(I(x,y;\epsilon)) = \int\int I(x,y;\epsilon) e^{2\pi i (xu+yv)}\, dx\, dy \tag{1}$$

Bremsstralhung equation:

$$I(x,y;\epsilon) = \frac{a}{4\pi R^2} \int_{\epsilon}^{\infty} N(x,y) \bar{F}(x,y,E) Q(\epsilon,E)\, dE \tag{2}$$

From photon to electron visibilities

Photon visibilities:

$$V(u,v;\epsilon) = \mathcal{F}(I(x,y;\epsilon)) = \int\int I(x,y;\epsilon)e^{2\pi i(xu+yv)}\,dx\,dy \tag{1}$$

Bremsstralhung equation:

$$I(x,y;\epsilon) = \frac{a}{4\pi R^2}\int_{\epsilon}^{\infty} N(x,y)\bar{F}(x,y,E)Q(\epsilon,E)\,dE \tag{2}$$

From photon to electron visibilities

Photon visibilities:

$$V(u,v;\epsilon) = \mathcal{F}(I(x,y;\epsilon)) = \int\int I(x,y;\epsilon)e^{2\pi i(xu+yv)}\,dx\,dy \qquad (1)$$

Bremsstralhung equation:

$$I(x,y;\epsilon) = \frac{a}{4\pi R^2}\int_\epsilon^\infty N(x,y)\bar{F}(x,y,E)Q(\epsilon,E)\,dE \qquad (2)$$

$$\boxed{N(x,y) = \int_0^{\ell(x,y)} n(x,y,z)\,dz}$$

$n(x,y,z)$ is the local density of target particles along the line-of-sight depth $\ell(x,y)$

$$\boxed{\bar{F}(x,y;E) = \frac{1}{N(x,y)}\int_0^{\ell(x,y)} n(x,y,z)F(x,y,z;E)\,dz}$$

$F(x,y,z;E)$ is the differential electron flux spectrum at the point (x,y,z)

From photon to electron visibilities

Photon visibilities:

$$V(u,v;\epsilon) = \mathcal{F}(I(x,y;\epsilon)) = \int\int I(x,y;\epsilon) e^{2\pi i(xu+yv)}\, dx\, dy \tag{1}$$

Bremsstralhung equation:

$$I(x,y;\epsilon) = \frac{a}{4\pi R^2} \int_{\epsilon}^{\infty} N(x,y)\bar{F}(x,y,E)Q(\epsilon,E)\, dE \tag{2}$$

Electron visibilities:

$$W(u,v,E) = \frac{a}{4\pi R^2} \int\int N(x,y)\bar{F}(x,y;E) e^{2\pi i(xu+yv)}\, dx\, dy \tag{3}$$

From photon to electron visibilities

Photon visibilities:

$$V(u, v; \epsilon) = \mathcal{F}(I(x, y; \epsilon)) = \int\int I(x, y; \epsilon) e^{2\pi i (xu + yv)} \, dx \, dy \tag{1}$$

Bremsstralhung equation:

$$I(x, y; \epsilon) = \frac{a}{4\pi R^2} \int_{\epsilon}^{\infty} N(x, y) \bar{F}(x, y, E) Q(\epsilon, E) \, dE \tag{2}$$

Electron visibilities:

$$W(u, v, E) = \frac{a}{4\pi R^2} \int\int N(x, y) \bar{F}(x, y; E) e^{2\pi i (xu + yv)} \, dx \, dy \tag{3}$$

Bremsstralhung equation for visibilities:

$$V(u, v; \epsilon) = \int_{\epsilon}^{\infty} W(u, v; E) Q(\epsilon, E) \, dE \tag{4}$$

From photon to electron visibilities

Photon visibilities:

$$V(u,v;\epsilon) = \mathcal{F}(I(x,y;\epsilon)) = \int\int I(x,y;\epsilon)e^{2\pi i(xu+yv)}\,dx\,dy \tag{1}$$

Bremsstralhung equation:

$$I(x,y;\epsilon) = \frac{a}{4\pi R^2}\int_{\epsilon}^{\infty} N(x,y)\bar{F}(x,y,E)Q(\epsilon,E)\,dE \tag{2}$$

Electron visibilities:

$$W(u,v,E) = \frac{a}{4\pi R^2}\int\int N(x,y)\bar{F}(x,y;E)e^{2\pi i(xu+yv)}\,dx\,dy \tag{3}$$

Bremsstralhung equation for visibilities:

$$\boxed{V(u,v;\epsilon)} = \int_{\epsilon}^{\infty} \boxed{W(u,v;E)}\,Q(\epsilon,E)\,dE \tag{4}$$

Measured photon visibilities

Electron visibilities

Visibility inversion algorithm - Photon visibilities

Photon visibilities

$$
\begin{array}{c|cccc|}
 & \varepsilon_1 & \varepsilon_2 & \cdots\cdots & \varepsilon_N \\
\hline
(u_1, v_1) & V_{1,1} & V_{1,2} & \cdots\cdots & V_{1,N} \\
(u_2, v_2) & V_{2,1} & V_{2,2} & \cdots\cdots & V_{2,N} \\
\vdots & \vdots & \vdots & \ddots & \vdots \\
(u_{N_V}, v_{N_V}) & V_{N_V,1} & V_{N_V,2} & \cdots\cdots & V_{N_V,N} \\
\hline
\end{array}
$$

Piana et al., *Electron flux spectral imaging of solar flares through regularized analysis of hard x-ray source visibilities,* The Astrophysical Journal, (2007)

Visibility inversion algorithm - Photon visibilities

Photon visibilities

$$
\begin{array}{c|cccc|}
 & \varepsilon_1 & \varepsilon_2 & \cdots & \varepsilon_N \\ \hline
(u_1, v_1) & V_{1,1} & V_{1,2} & \cdots & V_{1,N} \\
(u_2, v_2) & V_{2,1} & V_{2,2} & \cdots & V_{2,N} \\
\vdots & \vdots & \vdots & \ddots & \vdots \\
(u_{N_V}, v_{N_V}) & V_{N_V,1} & V_{N_V,2} & \cdots & V_{N_V,N} \\ \hline
\end{array}
$$

Piana et al., *Electron flux spectral imaging of solar flares through regularized analysis of hard x-ray source visibilities,* The Astrophysical Journal, (2007)

Visibility inversion algorithm - Photon visibilities

Photon visibilities

$$
\begin{array}{c|cccc|}
 & \varepsilon_1 & \varepsilon_2 & \cdots\cdots & \varepsilon_N \\
\hline
(u_1, v_1) & V_{1,1} & V_{1,2} & \cdots\cdots & V_{1,N} \\
(u_2, v_2) & V_{2,1} & V_{2,2} & \cdots\cdots & V_{2,N} \\
\vdots & \vdots & \vdots & \ddots & \vdots \\
(u_{N_V}, v_{N_V}) & V_{N_V,1} & V_{N_V,2} & \cdots\cdots & V_{N_V,N} \\
\hline
\end{array}
$$

May 7, 2021 – 18:51 UT

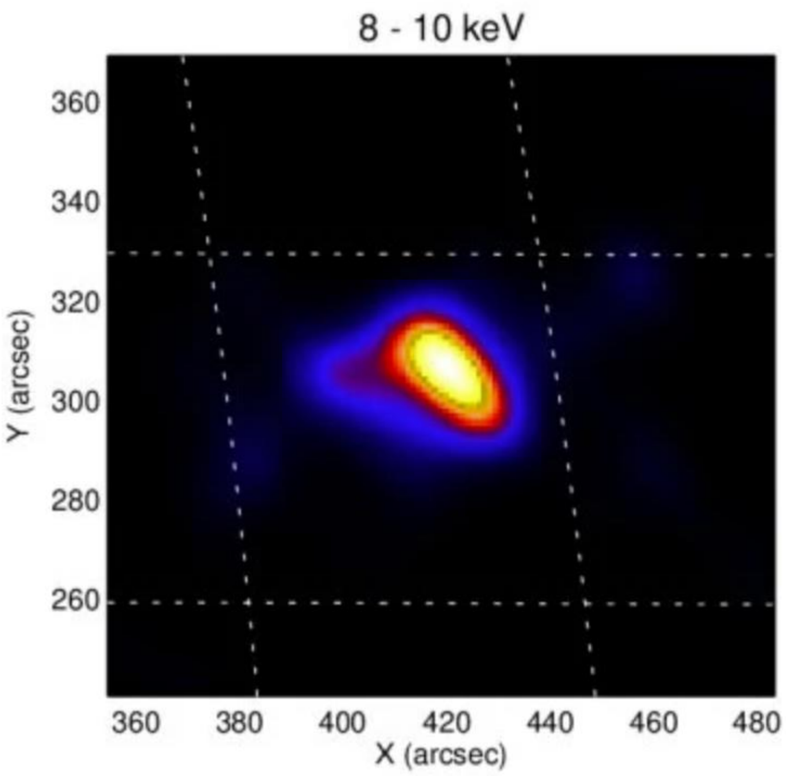

Figure: Reconstruction provided by MEM_GE, from photon visibilities.

Piana et al., *Electron flux spectral imaging of solar flares through regularized analysis of hard x-ray source visibilities,* The Astrophysical Journal, (2007)

Visibility inversion algorithm - Photon visibilities

Photon visibilities

$$
\begin{array}{c|cccc|}
 & \varepsilon_1 & \varepsilon_2 & \cdots\cdots & \varepsilon_N \\
\hline
(u_1, v_1) & V_{1,1} & V_{1,2} & \cdots\cdots & V_{1,N} \\
(u_2, v_2) & V_{2,1} & V_{2,2} & \cdots\cdots & V_{2,N} \\
\vdots & \vdots & \vdots & \ddots & \vdots \\
(u_{N_V}, v_{N_V}) & V_{N_V,1} & V_{N_V,2} & \cdots\cdots & V_{N_V,N} \\
\hline
\end{array}
$$

Piana et al., *Electron flux spectral imaging of solar flares through regularized analysis of hard x-ray source visibilities,* The Astrophysical Journal, (2007)

Visibility inversion algorithm - Photon visibilities

Photon visibilities

$$
\begin{array}{c|cccc|}
 & \varepsilon_1 & \varepsilon_2 & \cdots\cdots & \varepsilon_N \\
\hline
(u_1, v_1) & V_{1,1} & V_{1,2} & \cdots\cdots & V_{1,N} \\
(u_2, v_2) & V_{2,1} & V_{2,2} & \cdots\cdots & V_{2,N} \\
\vdots & \vdots & \vdots & \ddots & \vdots \\
(u_{N_V}, v_{N_V}) & V_{N_V,1} & V_{N_V,2} & \cdots\cdots & V_{N_V,N} \\
\hline
\end{array}
$$

May 7, 2021 – 18:51 UT

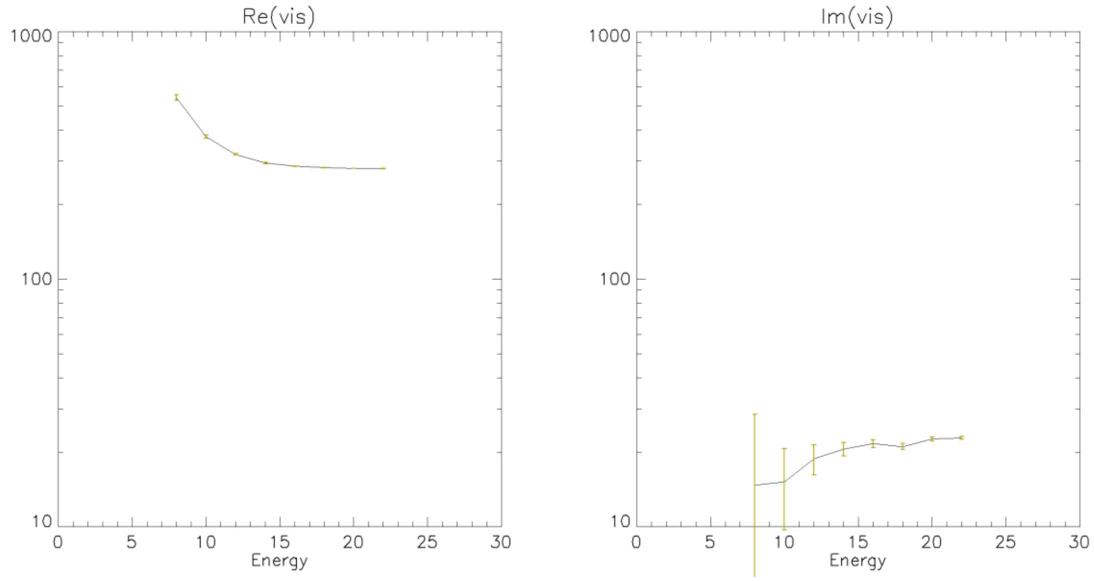

Figure: Real part (*on the left*) and imaginary part (*on the right*) of observed photon visibilities in $(u, v) = (0.002, -0.001)$ considering eight energy bands ($N = 8$).

Piana et al., *Electron flux spectral imaging of solar flares through regularized analysis of hard x-ray source visibilities,* The Astrophysical Journal, (2007)

Visibility inversion algorithm - Electron visibilities

Electron visibilities

$$
\begin{array}{cc}
 & \begin{array}{cccc} E_1 & E_2 & \cdots & E_M \end{array} \\
\begin{array}{c} (u_1, v_1) \\ (u_2, v_2) \\ \vdots \\ (u_{N_V}, v_{N_V}) \end{array} &
\begin{bmatrix}
W_{1,1} & W_{1,2} & \cdots & W_{1,M} \\
W_{2,1} & W_{2,2} & \cdots & W_{2,M} \\
\vdots & \vdots & \ddots & \vdots \\
W_{N_V,1} & W_{N_V,2} & \cdots & W_{N_V,M}
\end{bmatrix}
\end{array}
$$

Piana et al., *Electron flux spectral imaging of solar flares through regularized analysis of hard x-ray source visibilities,* The Astrophysical Journal, (2007)

Visibility inversion algorithm - Electron visibilities

Electron visibilities

$$
\begin{array}{c|cccc|}
 & E_1 & E_2 & \cdots & E_M \\
\hline
(u_1, v_1) & W_{1,1} & W_{1,2} & \cdots & W_{1,M} \\
(u_2, v_2) & W_{2,1} & W_{2,2} & \cdots & W_{2,M} \\
\vdots & \vdots & \vdots & \ddots & \vdots \\
(u_{N_V}, v_{N_V}) & W_{N_V,1} & W_{N_V,2} & \cdots & W_{N_V,M} \\
\hline
\end{array}
$$

Piana et al., *Electron flux spectral imaging of solar flares through regularized analysis of hard x-ray source visibilities,* The Astrophysical Journal, (2007)

Visibility inversion algorithm - Electron visibilities

Electron visibilities

$$
\begin{array}{c|c|ccc|}
 & E_1 & E_2 & \cdots\cdots & E_M \\
\hline
(u_1, v_1) & W_{1,1} & W_{1,2} & \cdots\cdots & W_{1,M} \\
(u_2, v_2) & W_{2,1} & W_{2,2} & \cdots\cdots & W_{2,M} \\
\vdots & \vdots & \vdots & \ddots & \vdots \\
(u_{N_V}, v_{N_V}) & W_{N_V,1} & W_{N_V,2} & \cdots\cdots & W_{N_V,M} \\
\hline
\end{array}
$$

May 7, 2021 – 18:51 UT

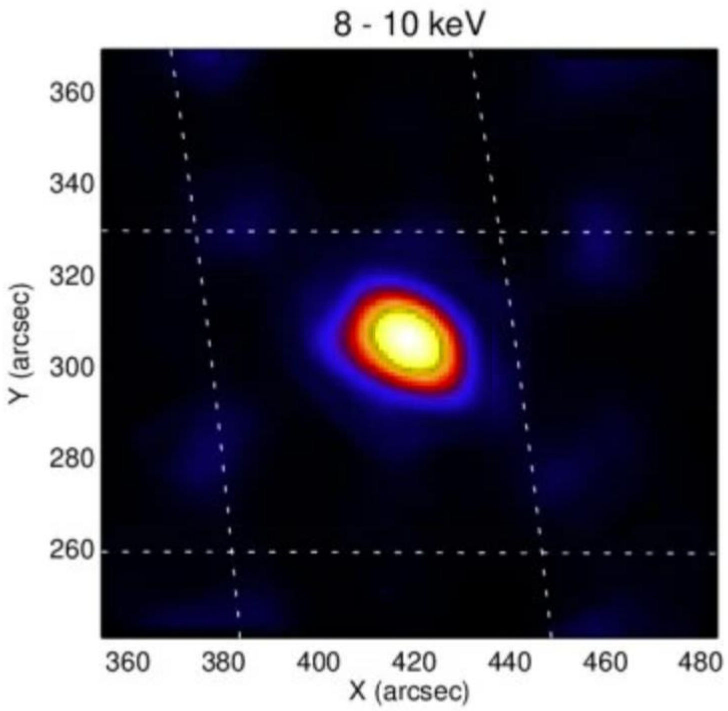

Figure: Reconstruction provided by MEM_GE, from electron visibilities.

Piana et al., *Electron flux spectral imaging of solar flares through regularized analysis of hard x-ray source visibilities,* The Astrophysical Journal, (2007)

Results – May 7, 2021

Photon images

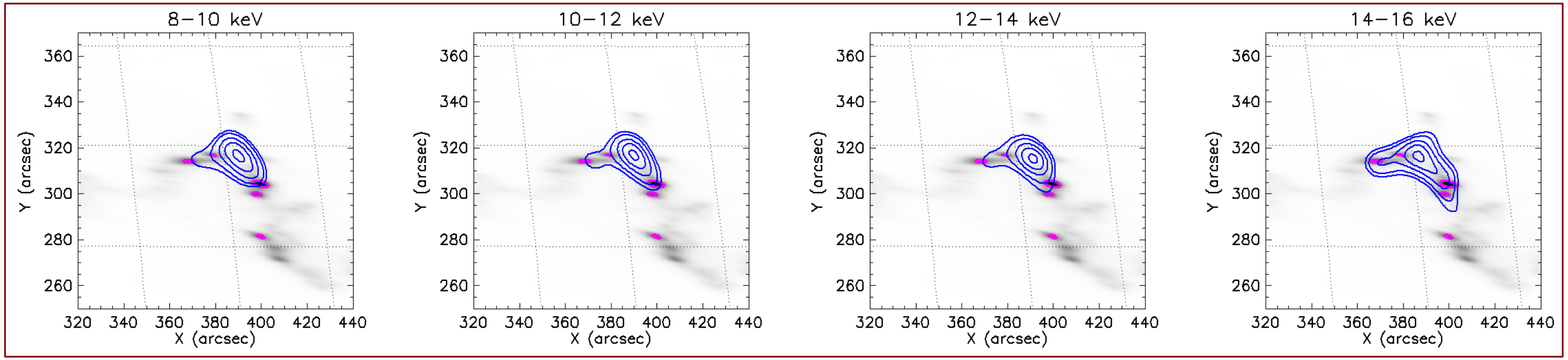

Electron flux images

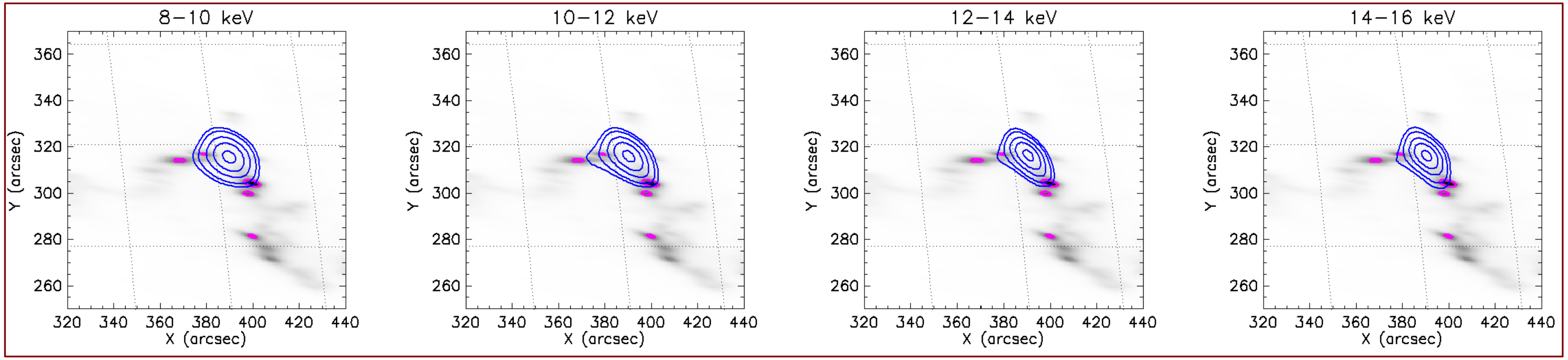

Figure: Photon images for the energy intervals shown (*top panels*), compared with the electron flux images corresponding to the regularized electron visibilities (*bottom panels*) in the same energy range. The 50% contour levels of the AIA images are plotted in magenta, while the 25, 35, 55, 75, 95% contour levels of the reconstructed map are plotted in blue. The maps are produced using the MEM-GE algorithm.

Results – May 7, 2021

Photon images

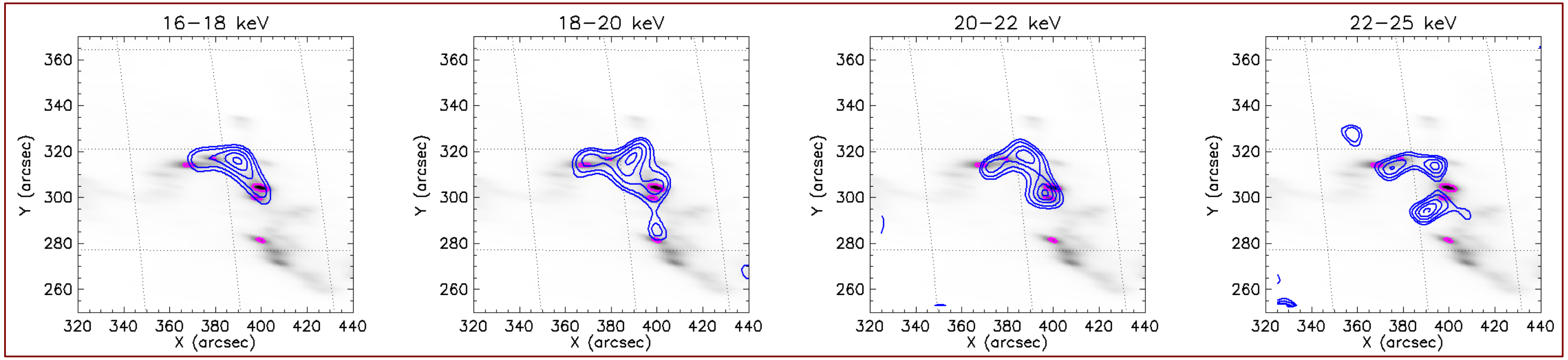

Electron flux images

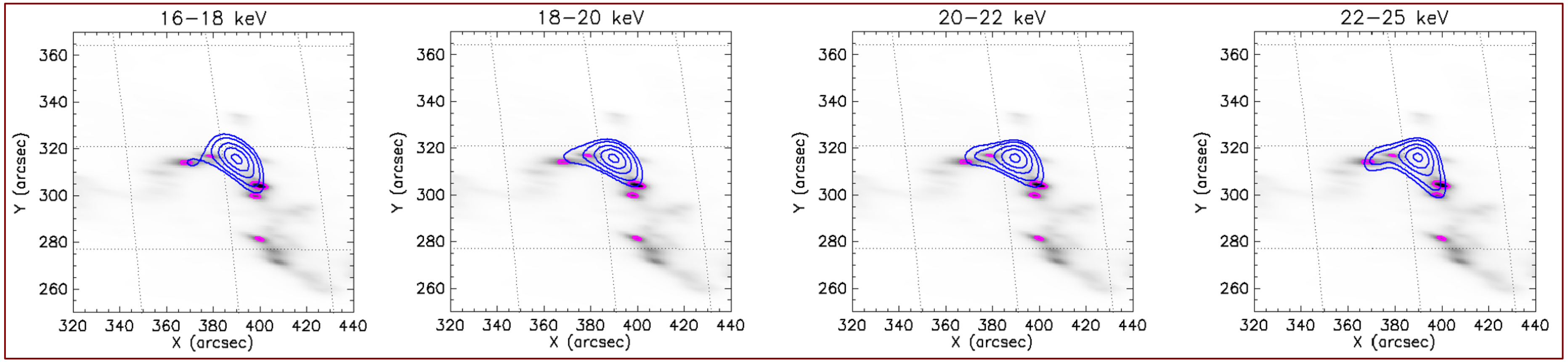

Figure: Photon images for the energy intervals shown (*top panels*), compared with the electron flux images corresponding to the regularized electron visibilities (*bottom panels*) in the same energy range. The 50% contour levels of the AIA images are plotted in magenta, while the 25, 35, 55, 75, 95% contour levels of the reconstructed map are plotted in blue. The maps are produced using the MEM-GE algorithm.

Results – May 7, 2021

Photon images

Electron flux images

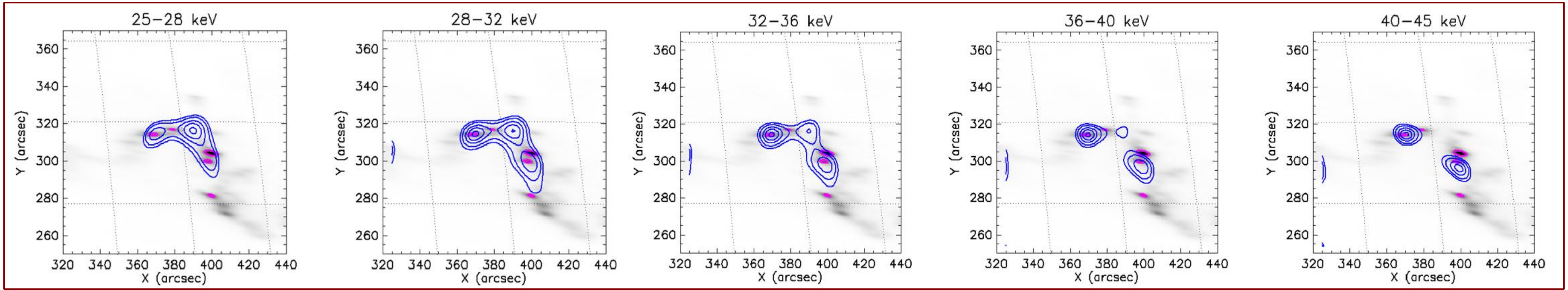

Figure: Photon images for the energy intervals shown (*top panels*), compared with the electron flux images corresponding to the regularized electron visibilities (*bottom panels*) in the same energy range. The 50% contour levels of the AIA images are plotted in magenta, while the 25, 35, 55, 75, 95% contour levels of the reconstructed map are plotted in blue. The maps are produced using the MEM-GE algorithm.

Results – May 7, 2021

Photon images

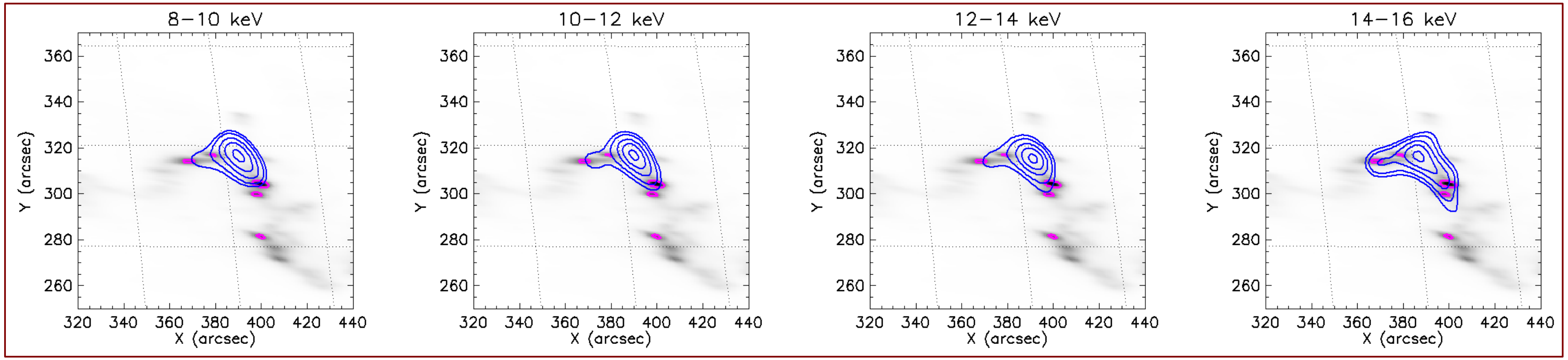

Regularized photon images

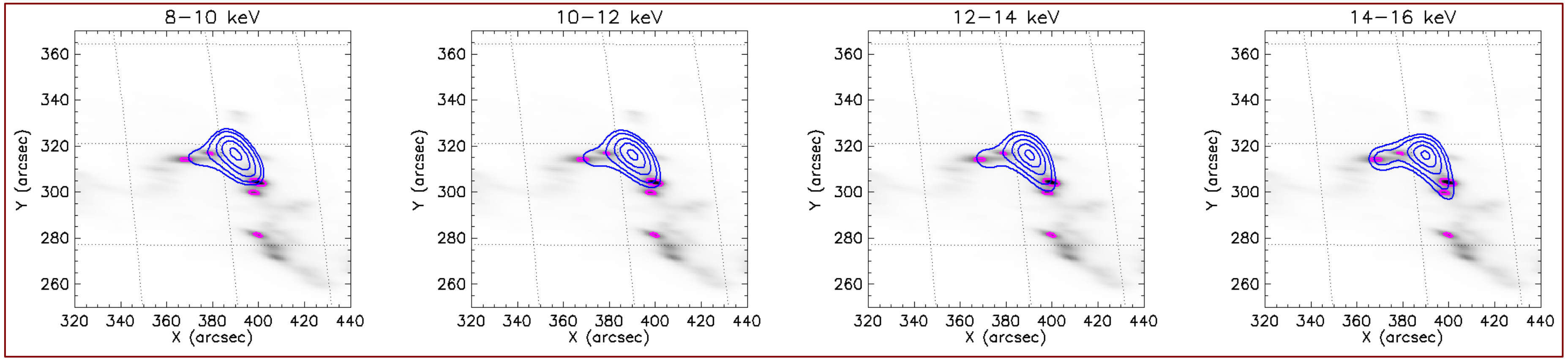

Figure: Photon images for the energy intervals shown (*top panels*), compared with the regularized photon-based images (*bottom panels*) in the same energy range. The 50% contour levels of the AIA images are plotted in magenta, while the 25, 35, 55, 75, 95% contour levels of the reconstructed map are plotted in blue. The maps are produced using the MEM-GE algorithm.

Results – May 7, 2021

Photon images

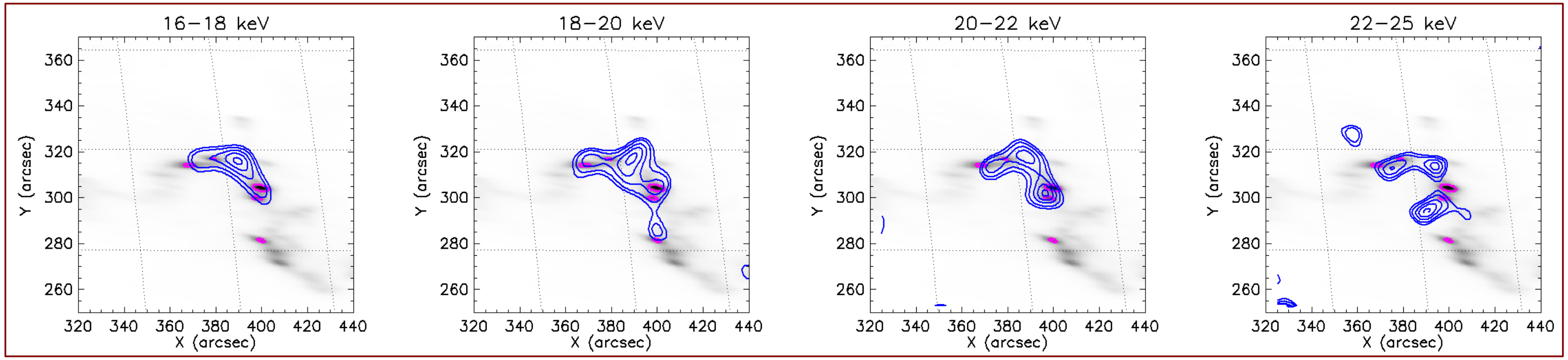

Regularized photon images

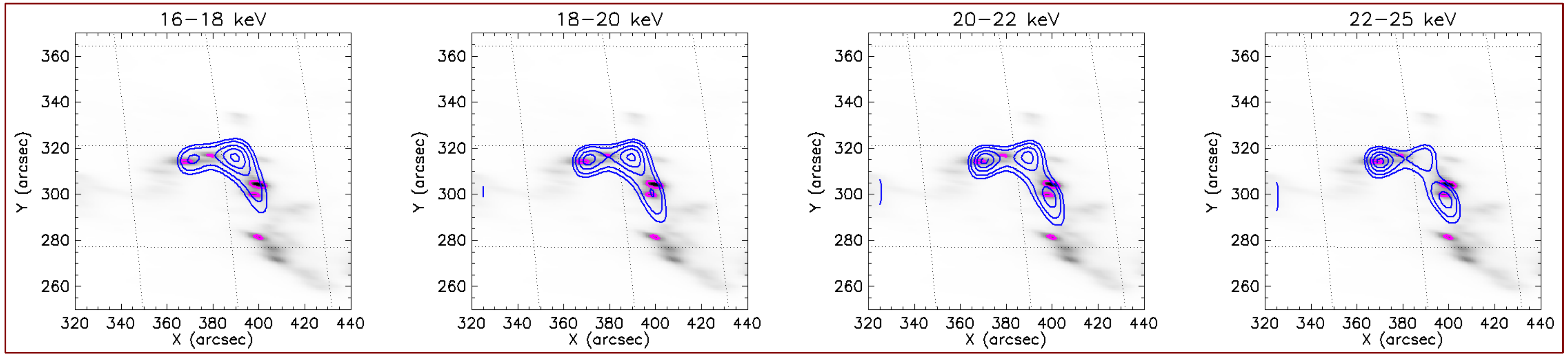

Figure: Photon images for the energy intervals shown (*top panels*), compared with the regularized photon-based images (*bottom panels*) in the same energy range. The 50% contour levels of the AIA images are plotted in magenta, while the 25, 35, 55, 75, 95% contour levels of the reconstructed map are plotted in blue. The maps are produced using the MEM-GE algorithm.

Results – May 7, 2021

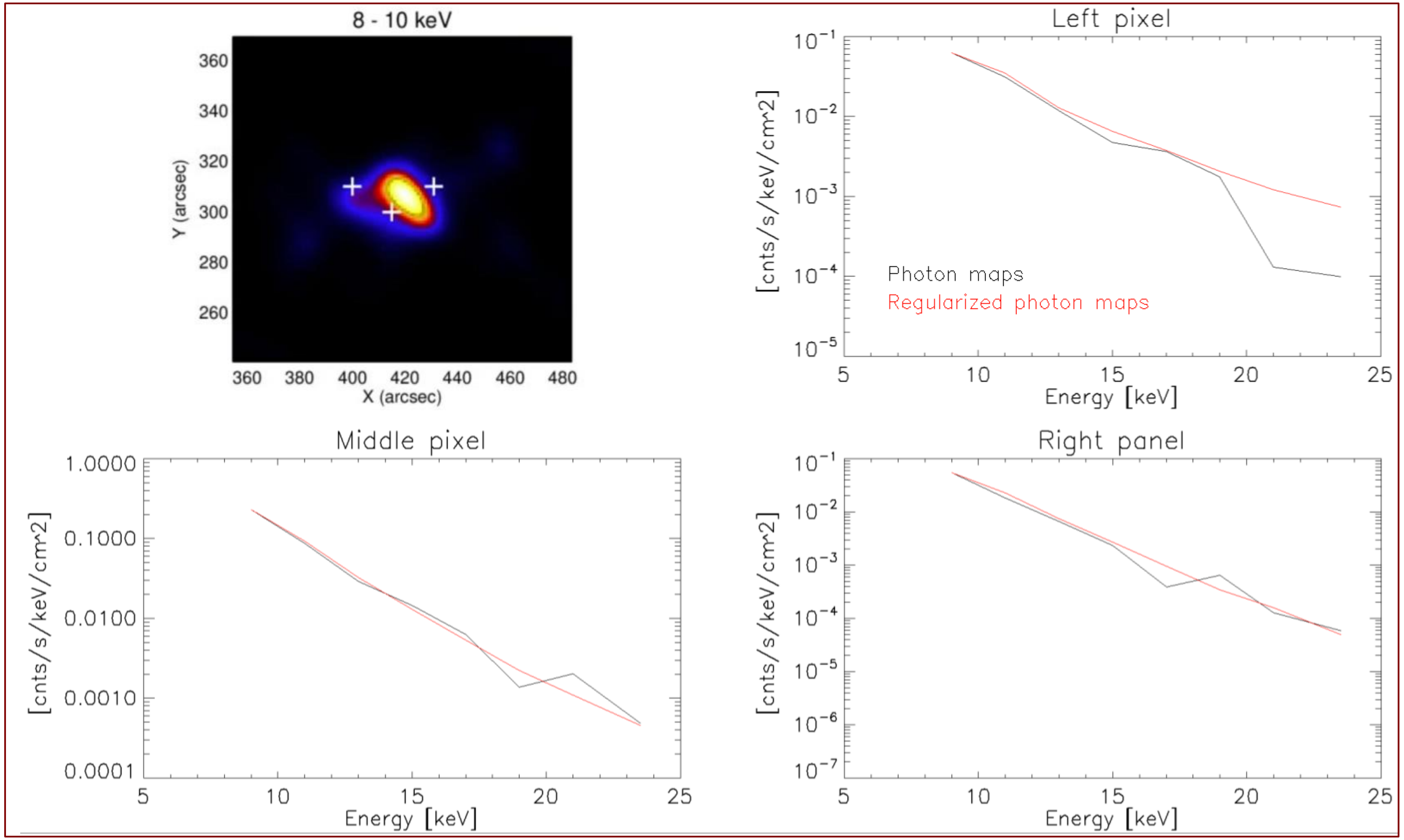

Figure: Pixel-wise spectrum obtained from photon maps and regularized photon maps. Top left panel: selected pixels are indicated with a white cross. Top right and bottom panels: pixel-wise spectrum (left, middle and right pixel highlighted in the top left panel, respectively) obtained from photon maps (*in black*) and regularized photon maps (*in red*). Plots are logarithmic scaled on the y-axis.

Results – May 7, 2021

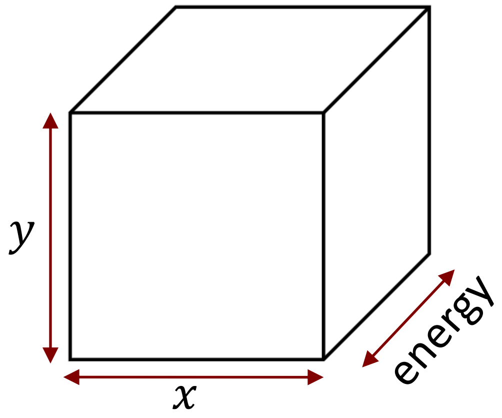

1. For each energy bin consider the total flux in the recovered map;
2. Consider the total flux as a function of the energy
3. Consider the flux spectrum provided by OSPEX

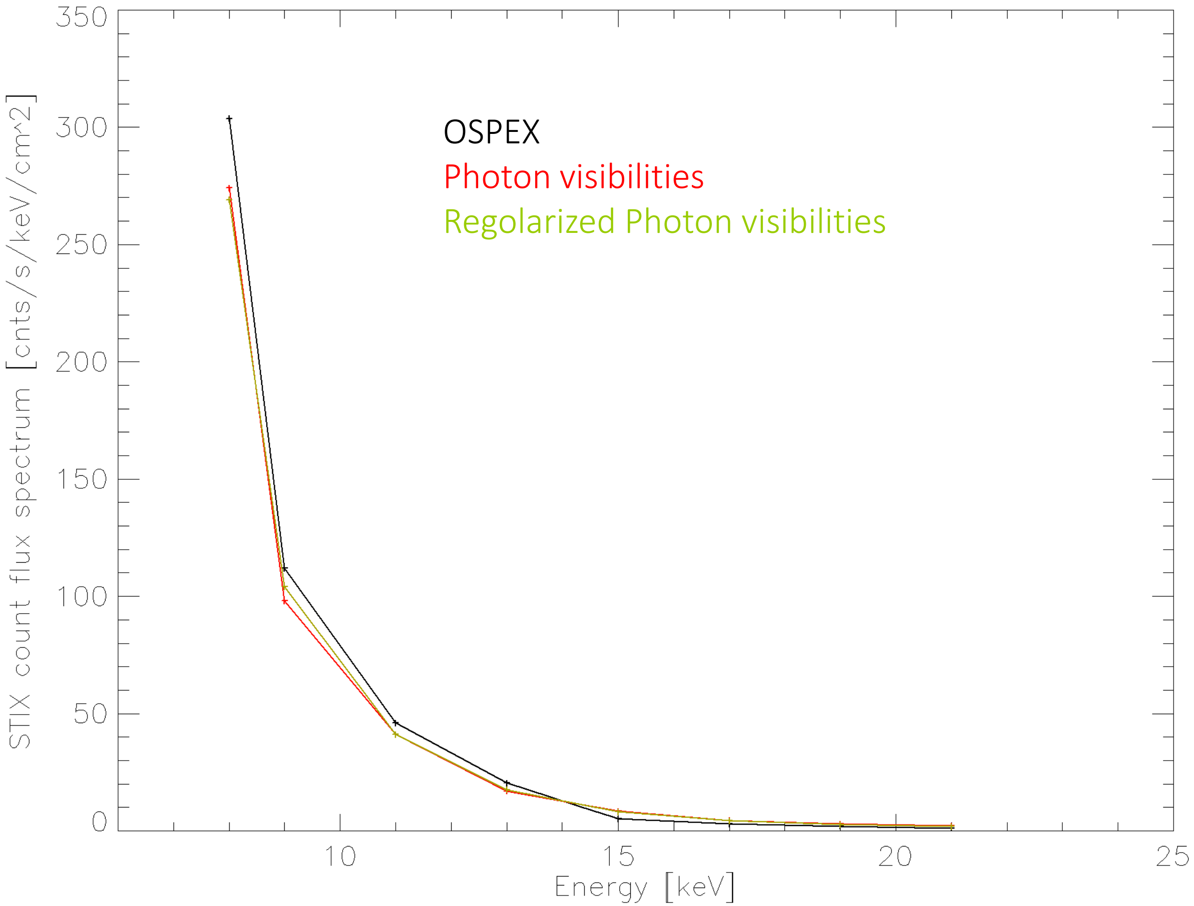

Figure: Total flux of the map reconstructed by MEM_GE, for May 7, 2021 event, considering photon visibilities (*in red*), regularized photon visibilities (*in green*), compared to OSPEX (*in black*).

Results – May 7, 2021

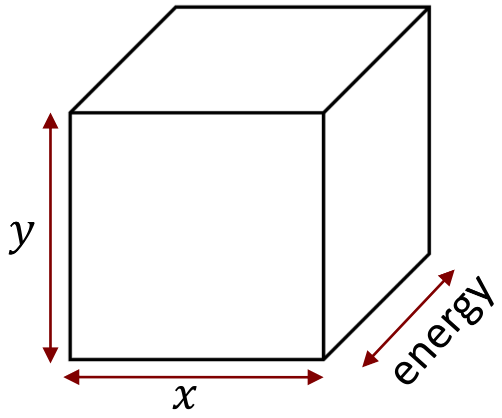

1. For each energy bin consider the total flux in the recovered map;
2. Consider the total flux as a function of the energy and fit with a power law
$$A\epsilon^{\gamma}$$
3. Consider the flux spectrum provided by OSPEX and fit it with a power law.

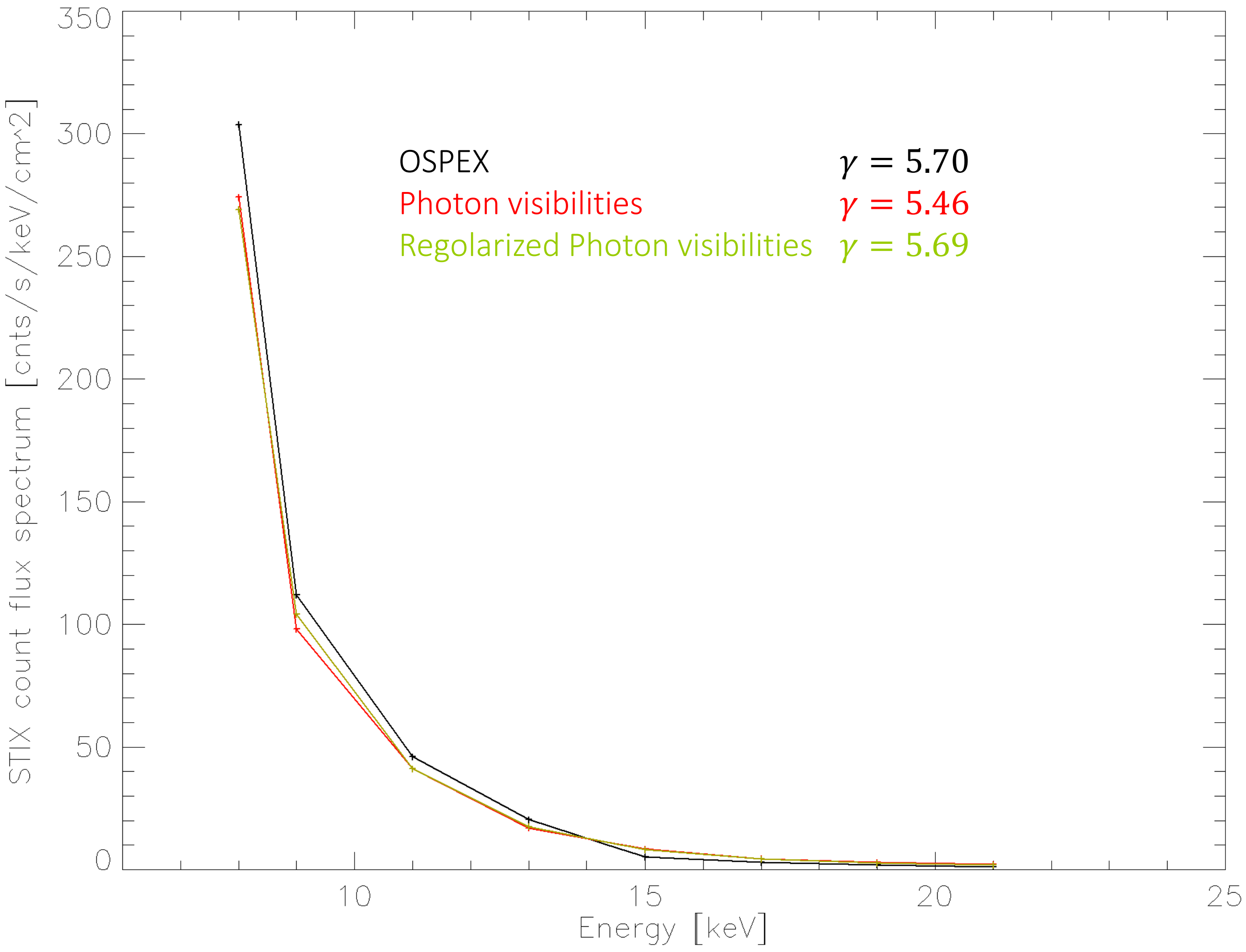

Results – May 7, 2021

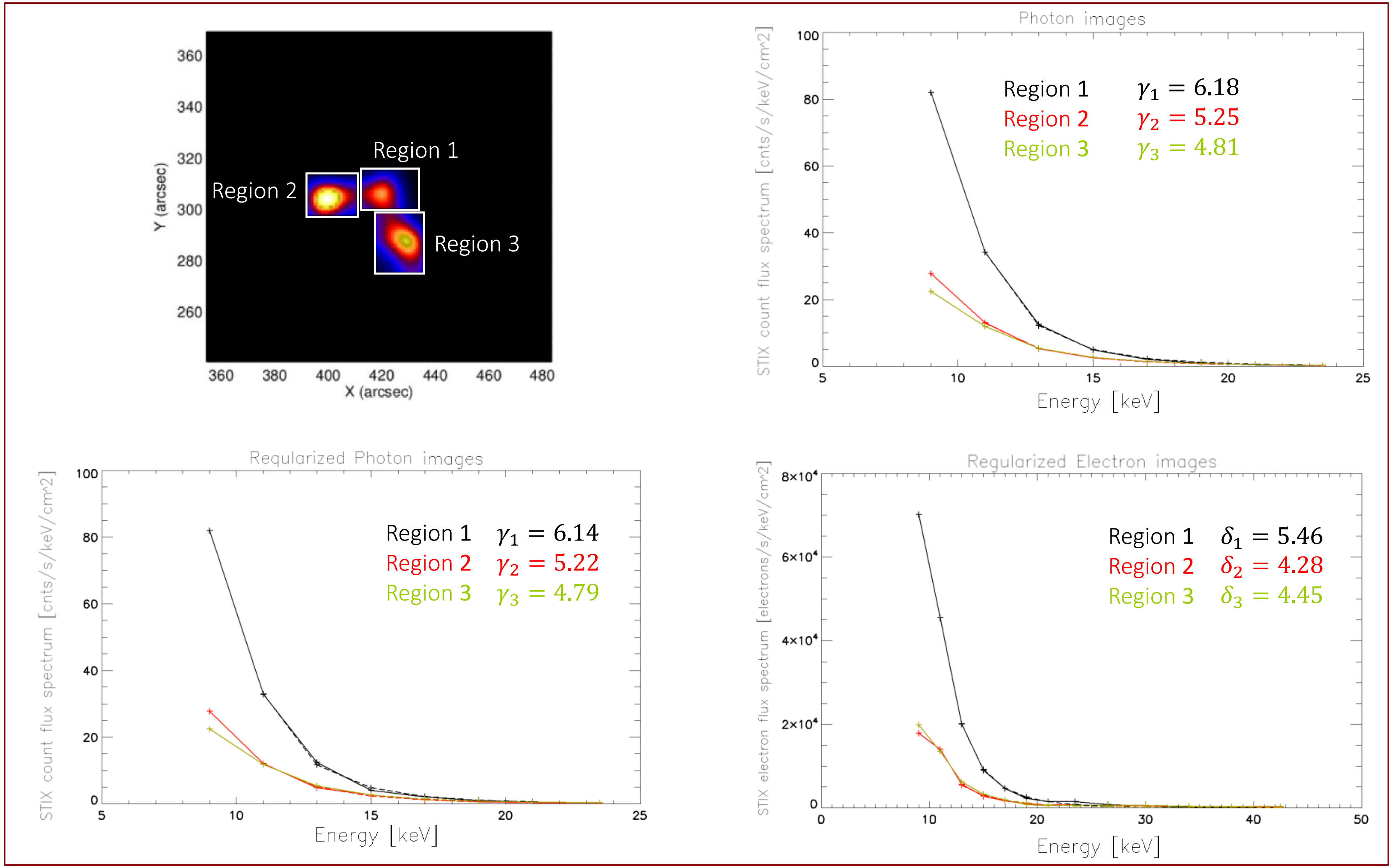

Figure: Top row: three selected subregions of the source (*left panel*) and STIX count flux spectrum and corresponding spectral index for the three selected subregions considering photon maps (*right panel*). Bottom row: STIX count flux spectrum and corresponding spectral index for the three selected subregions considering regularized photon maps (*left panel*) and the same in the case of electron flux spectrum (*right panel*).

Results – May 7, 2021

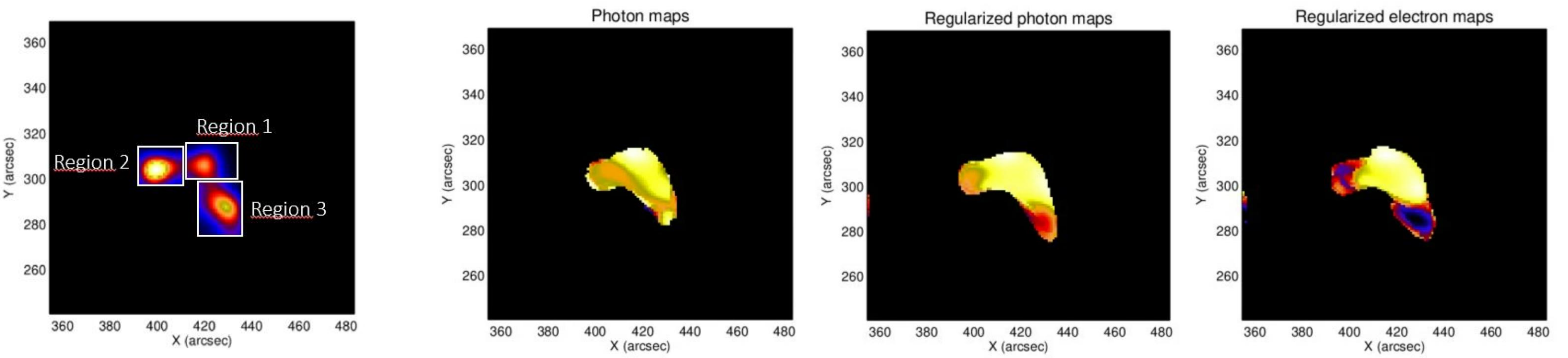

Figure: Left panel: three selected subregions of the source. Second, third and fourth panels show the pixel-wise spectral index for the three selected subregions considering photon maps, regularized photon maps and regularized electron maps, respectively.

Results – November 11, 2022

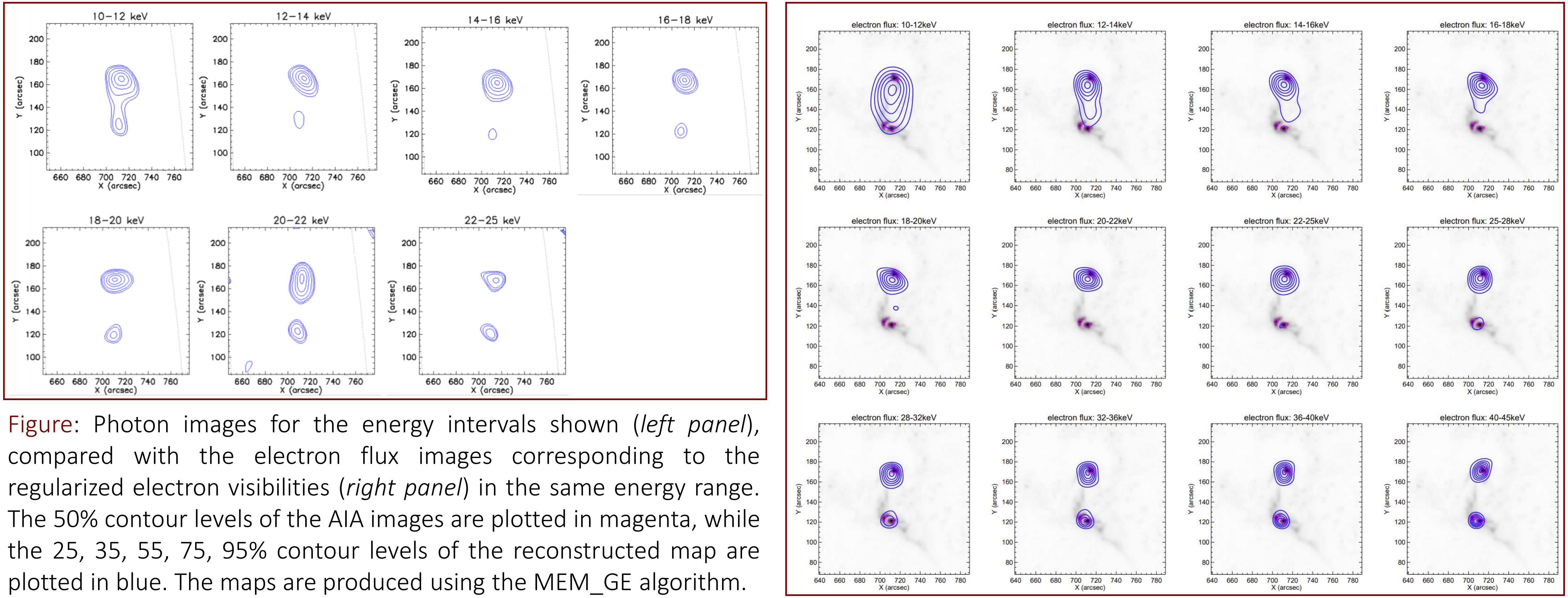

Figure: Photon images for the energy intervals shown (*left panel*), compared with the electron flux images corresponding to the regularized electron visibilities (*right panel*) in the same energy range. The 50% contour levels of the AIA images are plotted in magenta, while the 25, 35, 55, 75, 95% contour levels of the reconstructed map are plotted in blue. The maps are produced using the MEM_GE algorithm.

Results – November 11, 2022

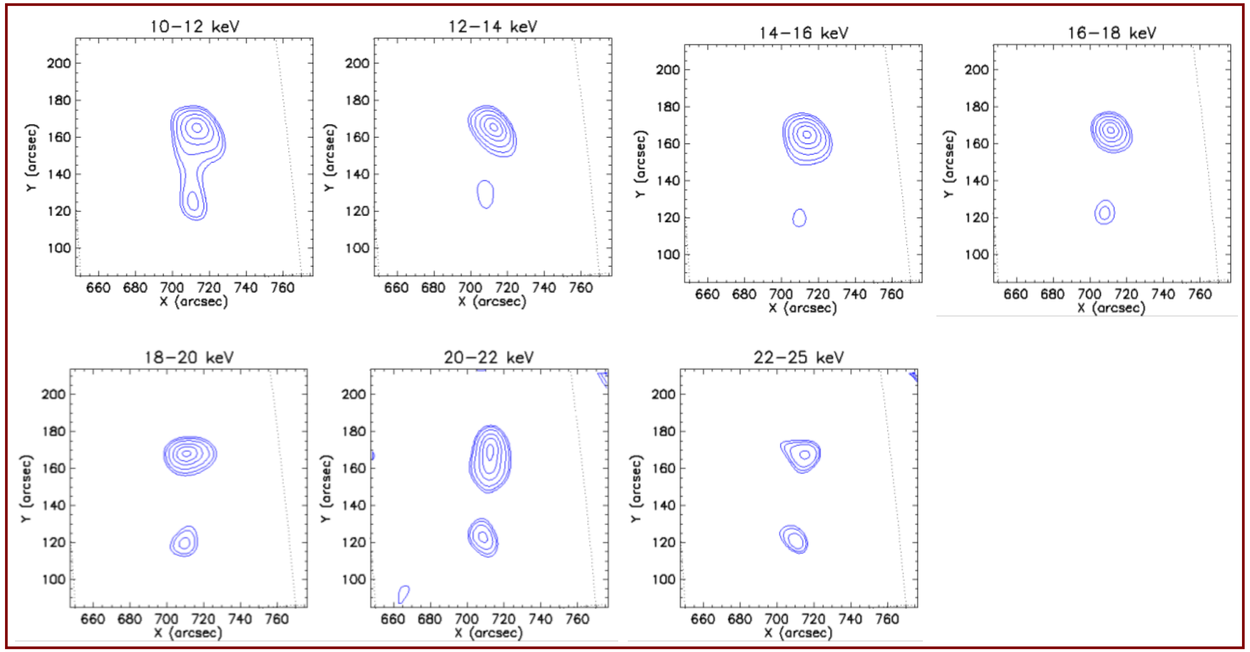

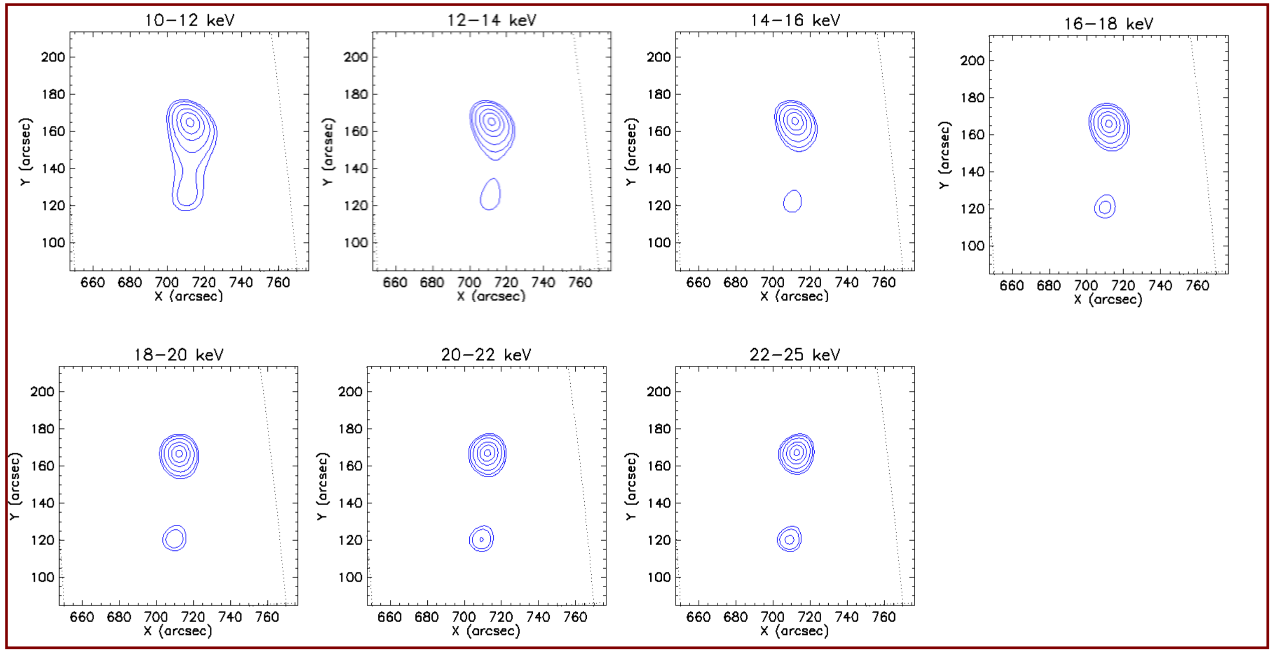

Figure: Photon images for the energy intervals shown (*left panel*), compared with the regularized photon-based images (*right panel*) in the same energy range. The 25, 35, 55, 75, 95% contour levels of the reconstructed map are plotted in blue. The maps are produced using the MEM_GE algorithm.

Results – November 11, 2022

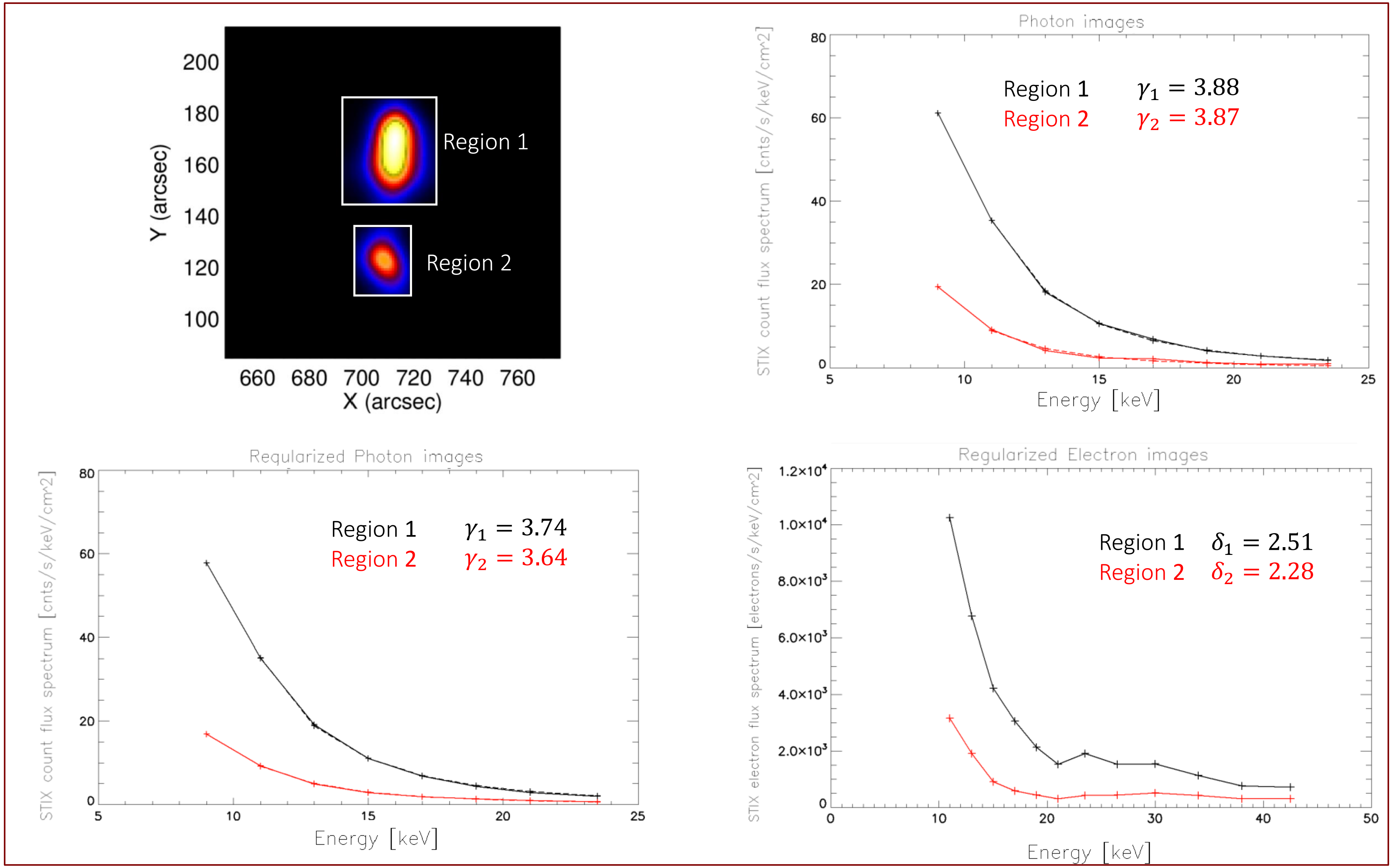

Figure: top row: two selected subregions of the source (*left panel*) and STIX count flux spectrum and corresponding spectral index for the two selected subregions considering photon maps (*right panel*). Bottom row: STIX count flux spectrum and corresponding spectral index for the two selected subregions considering regularized photon maps (*left panel*) and the same in the case of electron flux spectrum (*right panel*).

Results – May 7, 2021

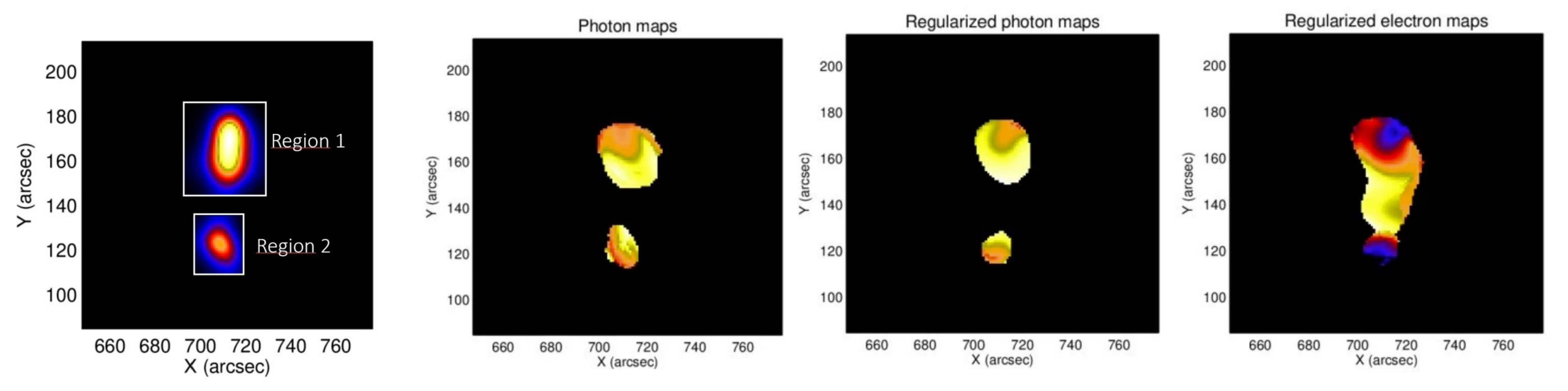

Figure: Left panel: two selected subregions of the source. Second, third and fourth panels show the pixel-wise spectral index for the two selected subregions considering photon maps, regularized photon maps and regularized electron maps, respectively.

Conclusions and future works

- ☑ We have described a new approach to solar hard X-ray imaging spectroscopy:
  - ☑ two-dimensional Fourier transforms of the image in the photon domain are transformed into Fourier transforms of the electron flux maps.
  - ☑ This tool also provides regularized photon visibilities corresponding to the regularized electron visibilities.

Conclusions and future works

- ☑ We have described a new approach to solar hard X-ray imaging spectroscopy:
    - ☑ two-dimensional Fourier transforms of the image in the photon domain are transformed into Fourier transforms of the electron flux maps.
    - ☑ This tool also provides regularized photon visibilities corresponding to the regularized electron visibilities.

- ☑ We have proved inhomogeneity of the spectral index considering two flares observed by STIX.

Conclusions and future works

- ☑ We have described a new approach to solar hard X-ray imaging spectroscopy:
    - ☑ two-dimensional Fourier transforms of the image in the photon domain are transformed into Fourier transforms of the electron flux maps.
    - ☑ This tool also provides regularized photon visibilities corresponding to the regularized electron visibilities.
- ☑ We have proved inhomogeneity of the spectral index considering two flares observed by STIX.
- ❑ We are working on the time variability of the spectral index.

Conclusions and future works

- ☑ We have described a new approach to solar hard X-ray imaging spectroscopy:
  - ☑ two-dimensional Fourier transforms of the image in the photon domain are transformed into Fourier transforms of the electron flux maps.
  - ☑ This tool also provides regularized photon visibilities corresponding to the regularized electron visibilities.
- ☑ We have proved inhomogeneity of the spectral index considering two flares observed by STIX.
- ❑ We are working on the time variability of the spectral index.
- ❑ We are working to take into account of both diagonal and non-diagonal terms of the DRM.

Conclusions and future works

- ☑ We have described a new approach to solar hard X-ray imaging spectroscopy:
  - ☑ two-dimensional Fourier transforms of the image in the photon domain are transformed into Fourier transforms of the electron flux maps.
  - ☑ This tool also provides regularized photon visibilities corresponding to the regularized electron visibilities.
- ☑ We have proved inhomogeneity of the spectral index considering two flares observed by STIX.
- ❑ We are working on the time variability of the spectral index.
- ❑ We are working to take into account of both diagonal and non-diagonal terms of the DRM.
- ❑ We are testing this approach on more events to include the codes in SSW-IDL.

References

- Brown et al., *Fast spectral fitting of hard X-ray bremsstrahlung from truncated power-law electron spectra*, Astronomy and Astrophysics, (2008)
- Emslie et al., *RHESSI hard x-ray imaging spectroscopy of the large gamma-ray flare of 2002 July 23,* The Astrophysical Journal, (2003)
- Krucker et al., *The Spectrometer/Telescope for Imaging X-rays (STIX),* Astronomy and Astrophysics, (2020)
- Massa et al., *First Hard X-Ray Imaging Results by Solar Orbiter STIX*, Solar Physics, (2022)
- Massa et al., *MEM_GE: A New Maximum Entropy Method for Image Reconstruction from Solar X-Ray Visibilities*, The Astrophysical Journal, (2020)
- Massa et al., *STIX imaging I – Concept*, arxiv, (2023)
- Massone et al., *Regularized solution of the solar Bremsstrahlung inverse problem: model dependence and implementation issues*, Inverse Problems in Science and Engineering, (2004)
- Piana et al., *Electron flux spectral imaging of solar flares through regularized analysis of hard x-ray source visibilities,* The Astrophysical Journal, (2007)
- Piana et al., *Hard X-rays imaging of Solar Flares*, Springer, (2022)
- Prato et al., *A Regularized Visibility-Based Approach to Astronomical Imaging Spectroscopy*, SIAM Journal on Imaging Sciences, (2009)

THANK YOU FOR THE ATTENTION!

volpara@dima.unige.it

Università di Genova
DIMA | Dipartimento di Matematica
MIDA group